Optimizing Upconversion Nanoparticles for FRET Biosensing

Federico Pini, Laura Francés-Soriano, Vittoria Andrigo, Marta Maria Natile, Niko Hildebrandt

Optimizing Upconversion Nanoparticles for FRET Biosensing

Federico Pini,[1,2,3] Laura Francés-Soriano,[1,4] Vittoria Andrigo,[2,3] Marta Maria Natile,[2,3*] Niko Hildebrandt[1,5*]

[1] *Laboratoire COBRA, Université de Rouen Normandie, CNRS, INSA Rouen, Normandie Université, 76000 Rouen, France.*
[2] *Istituto di Chimica della Materia Condensata e Tecnologie per l'Energia (ICMATE), Consiglio Nazionale delle Ricerche (CNR), 35131 Padova, Italy.*
[3] *Dipartimento di Scienze Chimiche, Università di Padova, 35131 Padova, Italy.*
[4] *Instituto de Ciencia Molecular (ICMol), University of Valencia, 46980 Valencia, Spain.*
[5] *Department of Chemistry, Seoul National University, Seoul 08826, South Korea.*

**Corresponding authors: martamaria.natile@unipd.it, niko.hildebrandt@univ-rouen.fr*

ABSTRACT. Upconversion nanoparticles (UCNPs) are one of the most promising nanomaterials for bioanalytical and biomedical applications. One important challenge to be still solved is how UCNPs can be optimally implemented into Förster resonance energy transfer (FRET) biosensing and bioimaging for highly sensitive, wash free, multiplexed, accurate, and precise quantitative analysis of biomolecules and biomolecular interactions. The many possible UCNP architectures composed of a core and multiple shells doped with different lanthanoid ions at different ratios, the interaction with FRET acceptors at different possible distances and orientations via biomolecular interaction, and the many and long-lasting energy transfer pathways from the initial UCNP excitation to the final FRET process and acceptor emission, make the experimental determination of the ideal UCNP-FRET configuration for optimal analytical performance a real challenge. To overcome this issue, we have developed a fully analytical model that requires only a few experimental configurations to determine the ideal UCNP-FRET system within a few minutes. We verified our model via experiments using nine different Nd, Yb, and Er doped core-shell-shell UCNP architectures within a prototypical DNA hybridization assay using Cy3.5 as an acceptor dye. Using the selected experimental input, the model determined the optimal UCNP out of all theoretically possible combinatorial configurations. An extreme economy of time, effort, and material was accompanied by a significant sensitivity increase, which demonstrated the powerful feat of combining a few selected experiments with sophisticated but rapid modeling to accomplish an ideal FRET biosensor.

KEYWORDS: *Upconverting nanocrystals, energy transfer, DNA, FRET, sensitivity, neodymium*

INTRODUCTION

Lanthanoid-doped upconversion nanoparticles (UCNPs) can convert near-infrared excitation into visible emission, leading to background-free photoluminescence.[1,2] This photophysical feature, combined with high photostability, the absence of photobleaching, and low toxicity,[3,4] has resulted in a broad application of UCNPs in biosensing,[5–9] bioimaging,[10–12] and theranostics.[13–17] The most commonly employed UCNPs consist of a $NaYF_4$ host matrix doped with Yb^{3+} ions (sensitizers) that absorb around 980 nm and Er^{3+} (or Tm^{3+}, Ho^{3+}) ions (activators), which produce the upconversion luminescence (UCL) in the ultraviolet-visible-near infrared (UV-VIS-NIR) spectral regions.[18–22] Owing to the very low overall UCL quantum yields, UCNPs require high-power excitation. This requirement can become a serious disadvantage because the absorption of water in the 980 nm region can result in heating and damage of biological samples and limits the light penetration depth.[23–25] One possibility to overcome this problem is the use of Nd^{3+} ions as sensitizers.[26] Not only do they absorb around 800 nm, where water absorption is strongly reduced, but they also have a higher absorption cross-sections than Yb^{3+}.[23,27,28] Unfortunately, Yb^{3+} cannot be simply replaced by Nd^{3+} and the design and optimization of Nd^{3+}-based UCNPs with efficient UCL is significantly more challenging.[12,29,30]

Another important level of complexity is added when UCNPs are applied in biosensing using Förster resonance energy transfer (FRET).[31,32] In principle, UCNP-FRET can merge the advantages of UCNPs for biosensing with the high sensitivity and simplicity of wash-free FRET assays.[25,33,34] The narrow and tunable emission bands of lanthanoids can be matched with many different FRET acceptors.[35,36] Moreover, different strategies for functional bioconjugation of DNA close to the UCNP surface have been developed to respect the strong distance dependence of FRET.[8,9,37–39] Such thin coatings with direct DNA surface-attachment have the potential to significantly improve UCNP-based FRET biosensing and bioimaging, which is strongly limited when thick protective shells, such as silica or polymer shells, are used. Considering the importance of different types of DNA and RNA as disease biomarkers,[40–43] UCNP-FRET is seemingly perfect to answer the increasing demand for nucleic acid-based clinical diagnostics.[44,45] However, for UCNP-FRET, the energy from the activator ions inside the UCNP must be transferred to suitable FRET acceptors outside the UCNP. Therefore, not the UCL of the entire UCNP, which consists of the overall emission from all activators distributed over the UCNP, but the UCL of each

individual activator ion and their distance to each individual FRET acceptor define the figure of merit concerning FRET biosensing. The main dilemma for such UCNP-FRET systems is that the bright activators in the center of the UCNP (well protected from the environment) are farthest from the FRET acceptors, whereas the activators right below the surface of the UCNP that are closest to the FRET acceptors are the least bright (efficiently UCL quenching by the surrounding solvent).[46] The many and multidirectional energy transfer pathways between the initial sensitizer excitation and the final activator emission or FRET to an acceptor make UCNP-based FRET even more complicated. FRET efficiencies depend on excitation power and time (e.g., pulsed or continuous-wave excitation) and cannot be easily quantified by steady-state and time-resolved detection or their combination. Different recent studies have tried to gain a deeper understanding of the UCNP-FRET related mechanisms by careful investigation of different excitation and detection modes as well as different UCNP architectures.[47,48]

The UCL of UCNPs has been optimized via sizes, shapes, ion doping ratios, and core/shell concepts.[49–55] However, considering the sophisticated FRET properties with UCNP donors, UCNPs for FRET biosensing requires a very different optimization strategy that takes into account both UCL and FRET and optimal UCL is not necessarily ideal for optimal FRET. Advanced modelling of UCL offers the possibility to better understand experimental results, extract fundamental properties of the investigated nanosystem, and predict expected properties for specific UCNP designs and syntheses.[3,30,52,56] Several different modelling strategies can be applied, including macroscopic (or rate-equation),[52,54,57] microscopic,[21,47] and (semi-)analytical[58,59] approaches. Each category has pros and cons, and combinations are also possible, depending on the focus of the investigation. For example, macroscopic approaches provide a precise description of the overall energy level dynamics and of their interactions but require very accurate modelling of the energy transfer (ET) network and precise assumptions of initial fit parameters.[60–62] Microscopic approaches can follow the state of each ion in the UCNP, ET step by ET step, but are computationally expensive and require advanced approaches, such as Monte Carlo simulations.[63–65] Analytical (or semi-analytical) approaches are usually the fastest and easiest in computational terms, with the possibility of processing tens of datasets in a few seconds. Moreover, easily determinable properties of the samples (e.g., size or doping ratio) can be directly linked to the final optical properties (e.g., UCL lifetimes or quantum yields).[66,67] However, they necessitate time-consuming physical/mathematical modelling and do not offer the level

of detail that the other approaches can provide concerning fundamental properties and mechanisms. Recently, Park et al. developed an analytical model that could accurately describe FRET from a Tm^{3+}-doped UCNP to a pH-sensitive dye attached to the UCNP surface.[58] The experimental FRET efficiencies for different UCNP radii and amounts of acceptor dyes were in very good agreement with the model, which could also predict an ideal UCNP radius to Förster distance ratio for maximized FRET efficiency. While this study showed that advanced modelling can be very useful to predict ideal UCNP properties for efficient FRET and biosensing, there is a clear need for developing a model that can account for the full range of physical processes occurring in the UCNP.

With the aim to optimize and better understand UCNP-FRET systems for application in biosensing and imaging, in this study we have developed a fully analytical model and tested it on nine DNA-functionalized Nd^{3+}, Yb^{3+}, Er^{3+} (for simplicity, we will omit the "3+" superscript of the trivalent lanthanoid ions hereafter) doped core-shell-shell UCNPs with different architectures (i.e., distribution of the ions within the core and shells), Er doping, and size of both the core and the shells. Using a prototypical FRET assay, DNA labeled with a FRET acceptor dye was hybridized to the complementary DNA on the UCNP surface. Quantification of the dye-DNA target was performed by measuring the intensity ratios of FRET-sensitized dye fluorescence and FRET-quenched Er UCL upon 808 nm and 980 nm excitation for the entire UCNP library. By fitting the experimental data of both Er UCL and dye fluorescence, the model could establish a clear relation between excitation wavelength, Er activator doping ratio, core size, active-shell thickness, and inert-shell thickness on the one and analytical performance of the assay on the other hand. The model was then used to predict the specific UCNP architecture to accomplish the best assay performance for both 808 and 980 nm excitation. It is worth noting, that the maximum absorption wavelength for Nd-doped nanoparticles is usually blueshifted from the 808 nm maximum absorption of Nd:YAG (e.g., ~796 nm for $NaYF_4$:Nd^{3+}).[28] However, 808 nm diode lasers (which are used for pumping Nd:YAG lasers) are easily available in many different configurations and, in particular, with high power output. Therefore, most laboratories (including ours) are using high power 808 nm diode lasers for exciting Nd-based UCNPs. Although this wavelength is not ideal, it is still within the absorption band of $NaYF_4$:Nd^{3+}.

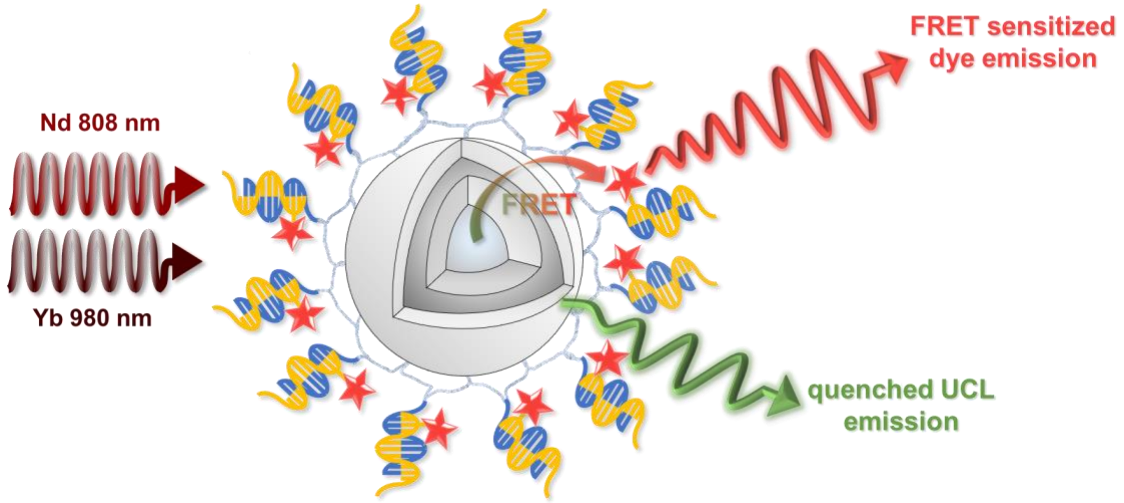

Figure 1. Prototypical UCNP-dye FRET DNA assay: DNA labeled with a FRET acceptor dye (yellow DNA with red star) hybridized to the complementary DNA (blue) on the UCNP surface. Upon excitation of Nd (808 nm) or Yb (980 nm) sensitizers, FRET from Er activators to dyes resulted in FRET-quenched UCL and FRET-sensitized dye fluorescence.

RESULTS AND DISCUSSION

Model design for UCNP-to-dye FRET DNA hybridization assays. The implementation of a model system as similar as possible to real-scenario FRET assays is a fundamental step to gain useful insights in the real working principles of such systems. For this reason, using a recently developed DNA-UCNP bioconjugation strategy for functional FRET assays,[9] we attached probe DNAs (DNA_1) on the UCNP surface. These probes were complementary to target DNAs labeled with Cyanine 3.5 dyes (DNA_2-Cy3.5). Hybridization of DNA_1 and DNA_2-Cy3.5 resulted in the formation of UCNP-Cy3.5 FRET pairs, which could be analyzed by measuring the FRET-quenched UCL and the FRET-sensitized dye emission upon 808 nm or 980 nm excitation (**Figure 1**). In this prototypical assay, the concentration (c) of the DNA_2-Cy3.5 target was thus quantified via the FRET ratio ($F_R(c)$ – equation 1):

$$F_R(c) = \frac{I_A(c)}{I_D(c)} = \frac{\int I_A^t(c)dt}{\int I_D^t(c)dt} \qquad (1)$$

where the intensity ratio of FRET-sensitized dye acceptor fluorescence (I_A) and FRET-quenched UCNP donor UCL (I_D) was obtained by integrating the time-resolved luminescence intensities I_A^t and I_D^t from t = 80 µs to t = 500 µs after the start of a 80 µs long excitation pulse (i.e., only the luminescence decays were integrated).

Hypothesizing a linear concentration dependence of $F_R(c)$, the slope of the calibration curve presents the analytical sensitivity (S) of the assay, which can be expressed by equation 2:

$$S = \frac{\partial F_R}{\partial c} = \frac{F_R(c)}{c} = \frac{1}{c}\left(\frac{I_A(c)}{I_D(c)}\right) = \frac{1}{c}\left(\frac{I_D^0 E_{FRET}^c \phi_A}{I_D^0(1-E_{FRET}^c)\phi_D}\right) = \frac{\phi_A}{\phi_D\, c}\left(\frac{E_{FRET}^c}{1-E_{FRET}^c}\right) = \frac{\phi_A\, k_{FRET}^c}{\phi_D\, c\, k_{tot}^{Er}} \quad (2)$$

Due to the linearity of the calibration curve, which starts at c = 0 and F_R = 0, the differentials can be substituted by F_R at a given c in the numerator and by c the denominator. Because the dye cannot be directly excited in the NIR, no dye background fluorescence can interfere with the measurement (assay tests containing only the dye were conducted and no luminescence was registered). Thus, both I_A and I_D can be written as a function of the initial Er donor luminescence intensity without FRET (I_D^0) and the FRET efficiency (E_{FRET}^c). In the case of FRET, I_D decreases with E_{FRET} (i.e., $I_D(c) = I_D^0(1 - E_{FRET}^c)\phi_D$), whereas I_A increases with the same amount that I_D decreases multiplied by the fluorescence quantum yield of the acceptor ϕ_A (i.e., $I_A(c) = I_D^0 E_{FRET}^c \phi_A$). Considering that the FRET efficiency is the ratio of FRET rate constant and the sum of FRET rate constant plus the total donor rate constant (i.e., $E_{FRET}^c = k_{FRET}^c/(k_{tot}^{Er} + k_{FRET}^c)$), the sensitivity can be expressed as an equation of dye and Er luminescence quantum yields, dye concentration, and rate constants as shown on the right side of equation 2. The total donor rate constant (or inverse donor UCL decay time τ_{Er}) can be expressed by equation 3:

$$\tau_{Er} = \left(k_{tot}^{Er}\right)^{-1} = \left(k_0^{Er} + k_Q^{Er} + k_{CR}^{ErEr} + k_{CR}^{ErNd} + k_{ET}^{ErYb}\right)^{-1} \quad (3)$$

It includes the rate constants of Er emission in the absence of any other ions (k_0^{Er}), environmental quenching of Er (k_Q^{Er}), Er-to-Er and Er-to-Nd cross-relaxation (k_{CR}^{ErEr}, k_{CR}^{ErNd}), and Er-to-Yb energy transfer (k_{ET}^{ErYb}). Equations 2 and 3 depend on the number of Er ions in the green-emitting state, which is a function of the Yb-to-Er ET efficiency (E_{ET}^{YbEr}) that also depends on the interactions with the other ions (Nd-to-Yb and Yb-to-Er energy transfer (k_{ET}^{NdYb}, k_{ET}^{YbEr}), and Yb-to-Yb energy migration (k_{mig}^{YbYb})) as well as on the environmental quenching of Yb and Nd (k_Q^{Yb}, k_Q^{Nd}). The result is a complex (though analytical) inter-dependence between the lanthanoid ions. Each k term in equations 2 and 3 was derived analytically according to the UCNP configuration (i.e., architecture, doping ratios, and lattice structure). The FRET and quenching terms were obtained by considering the sum of all ET steps between the multiple lanthanoid ion donors and the dye acceptors and quenchers on the UCNP surface. Similarly,

the ion-ion interactions were obtained by considering the sum of all ET steps to or from the other lanthanoid ions in the surrounding. All analytically derived fit parameters were then used to fit the experimental UCL decay times (equation 3) and FRET assay sensitivities (equation 2) for all UCNPs excited at 980 and 808 nm. The fit results could then be used to predict decay times and sensitivities for arbitrarily designed UCNPs. The complete model (including all equations for the different rate constants and the implementation of the structural UCNP parameters) is described in the Supporting Information (**Supporting Figure S1** and **Supporting Equations S1 to S25**). With the translation of the model in a Python program, several experimentally determined sensitivities and UCL decay times can be fit simultaneously using equations 2 and 3.

UCNPs design and experimental determination of UCL decays and FRET assay sensitivities. When designing UCNPs with Nd sensitizers, one must keep in mind that ET from Nd to Er is unfortunately very inefficient because cross-relaxation (CR) between these two ions is quite efficient.[27,29,37] Therefore, 808 nm excitable UCNPs are usually prepared by spatially separating Nd and Er in different compartments (core or shells) and by co-doping with Yb to bridge the excitation between the initial Nd sensitizers and the Er activators. Moreover, an optically inert (without sensitizer and activator ions) outer shell is usually added to minimize UCL environmental quenching, which becomes particularly important in aqueous media. Very thick shells can dramatically increase the UCL quantum yield but also significantly decrease the strongly distance-dependent FRET efficiency.[68,69] Hence, one needs to find an optimal shell thickness, at which the two effects are well balanced.

Following these general guidelines, we devised nine different sub-20 nm diameter UCNPs with two different configurations (**Figure 2**) to test our model. The "standard" (ST) configuration was similar to the well-studied $NaYF_4$:Yb,Er UCNPs, consisting of an emitting core (containing 20% Yb and variable amount of Er), surrounded by an absorbing shell (containing 20% Nd and 20% Yb), and protected by an undoped shell of $NaYF_4$. The "inverted" (IV) configuration comprised an absorbing core (20% Nd, 20% Yb), an emitting shell (20% Yb, variable amount of Er), and a protective undoped $NaYF_4$ shell (**Figure 2A**). Considering that co-doping of 2% Er with 20% Yb was found to be somewhat optimal for $NaYF_4$:Yb,Er UCNPs[70] but also taking into account that higher concentrations of Er in a shell may still result in sufficiently large Er-Er distances for suppressing CR, 2%,

5%, and 10% were selected as variable Er fractions for both the ST (ST02, ST05, and ST10) and IV (IV02, IV05, and IV10) UCNPs. Moreover, three IV02 UCNPs were prepared with a large core (IV02-C), a thick emitting shell (IV02-S1), and a thick inert shell (IV02-S2), respectively (**Figure 2B**).

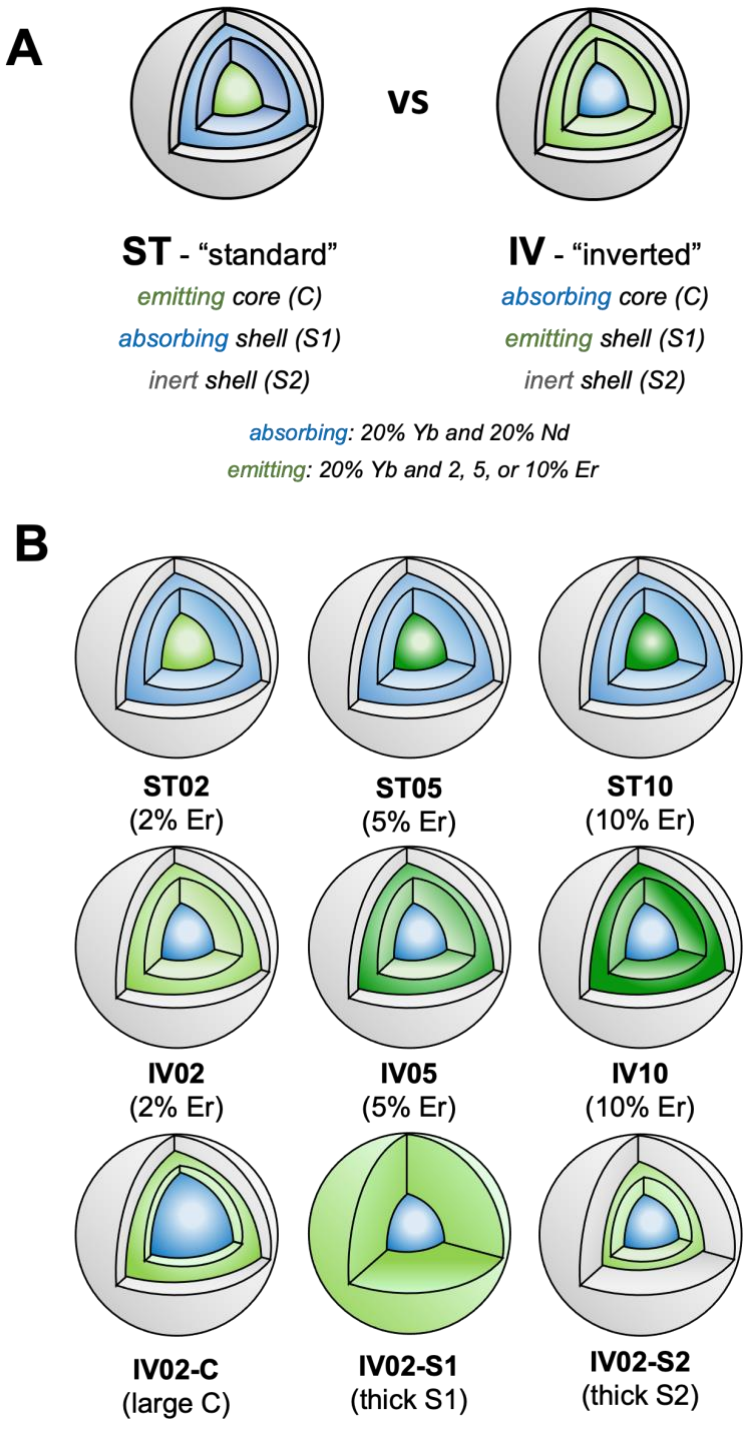

Figure 2. A: Two different core/shell/shell configurations for Nd, Yb, Er doped UCNPs used in this study. **B:** Nine different UCNPs that followed the two configurations from A were synthesized. The sizes of core and shells can slightly differ within the same ST and IV configurations (see **Table S1**).

All UCNPs were synthesized by similar procedures, differing only in the first shell addition (see **Materials and Methods** section for details).[71] Briefly, the initial core was obtained by coprecipitation, whereas the first shell was added by a seeded growth procedure (adding the core to a reaction mixture containing the shell precursor salts) for IV NPs or by Ostwald ripening of small Yb, Nd-doped sacrificial α-NPs hot-injected after the formation of the β-core for ST NPs. Similarly, for both configurations a protective shell was grown by hot-injection method but using undoped α-$NaYF_4$ sacrificial NPs. The composition and sizes of the nine different UCNPs are summarized in **Table S1**. The full characterization of the different UCNPs, including transmission electron microscopy (TEM – **Supporting Figure S2**), powder X-ray diffraction (PXRD – **Supporting Figure S3, Table S2**), steady-state UCL (**Supporting Figure S4**), and time-resolved UCL (**Supporting Figures S5 and S6**), is described in the **Supporting Information**.

For DNA bioconjugation to the UCNP surface, first the oleate ligands on the as prepared UCNPs were replaced sequentially by tetrafluoridoborate anions (obtaining BF_4-coated UCNPs) and by poly-sodium 4-styrenesulfonate (PSS).[72] The sulphonate groups ($-SO_3^-$) on the PSS have the triple function to i) anchor the polymer on the UCNP surface, ii) make the UCNPs hydrophilic, and iii) provide functional groups for the attachment of amino-terminated DNA (hereafter DNA_1) by a sulphonamide bond.[72] To satisfy the strong distance dependence of FRET, the 16 nucleotides (nt) DNA_1 (including a C_3 spacer) was attached on its 5' end (sulphonamide bond between a sulphonate group on the PSS and the amino group on DNA_1) to the UCNP@PSS, whereas Cy3.5 was directly attached to the 3' end of the fully DNA_1-complementary 16 nt DNA_2 (see **Table 2** for DNA sequences). Therefore, the UCNP surface and Cy3.5 were in principle separated only by the thin PSS shell (~2 nm) and the C_3 spacer (~1 nm).[9] UCNPs prepared with those thin PSS shells and bioconjugated with DNA previously showed good stability without significant aggregation over up to two weeks and were successfully applied in DNA and RNA FRET assays.[9,72] The UCL kinetics (at 540 nm) of all DNA_1 functionalized UCNPs (UCNP@PSS-DNA_1) were analyzed in HEPES buffer using both 980 nm and 808 nm excitation (**Supporting Figure S7** and **Supporting Table S3**). Long 80 µs excitation pulses were used to reach intensity saturation and measure only the UCL decays of the different UCNPs, which were fitted with mono-exponential functions (see **Materials and Methods** for details).[73]

We selected Cy3.5 as FRET acceptor because its absorption provides excellent spectral overlap with the green UCL band of the Er donor and its fluorescence can be detected without Er UCL background between the green and red UCL bands (**Figure 3A**). The assays were performed on a time-resolved fluorescence plate reader in 96-well microplates with 150 µL volume per well and consisted of UCNP@PSS-DNA_1 at constant concentration (1 $mg \cdot mL^{-1}$) and target DNA_2-Cy3.5 at different concentrations (0, 10, 20, 30, 40, or 50 $nmol \cdot L^{-1}$). Time-resolved UCNP donor UCL and Cy3.5 acceptor fluorescence were collected in parallel in independent detection channels (see **Figure 3A** for spectral bandwidth).

Increasing concentrations of DNA_2-Cy3.5 resulted in weak UCL intensity quenching of UCNPs (**Figure 3B** top) because only the Er ions in a FRET distance range to the dyes were quenched. However, the dye fluorescence showed a strong FRET sensitization from the UCNPs (**Figure 3B** bottom), as expressed by the very long fluorescence decay over several hundreds of microseconds (due to sensitization from the long-lived excited states of Er) and a DNA_2-Cy3.5 concentration-dependent intensity increase. The UCL decay times were not concentration dependent, which is not untypical when UCNPs are used as FRET donors. Recent studies showed that the luminescence decay time is not a reliable parameter for analyzing UCNP-based FRET because the energy stored in the Yb sensitizer ions is continuously transferred to the Er activators during the Er-to-dye FRET process.[39,48] Therefore, FRET does not significantly influence the overall decay time that depends on both the incoming and the outgoing energy contributions and is mainly driven by the slow energy transfer from Yb to Er. The assay calibration curves (FRET ratio from equation 1 with donor and acceptor luminescence intensities integrated in a time range from 80 µs to 500 s after the start of the excitation pulsed as a function of DNA_2-Cy3.5 concentration – **Figure 3C** and **Supporting Figure S8**) showed a linear increase over the entire concentration range, demonstrating that the hybridization assays were functional for DNA_2-Cy3.5 quantification. The sensitivities (slopes of the calibration curves) of all 18 assays (two excitation wavelengths and nine different UCNPs – **Figure 3D**) presented significant differences. In general, the sensitivities for 808 nm excitation were lower compared to 980 nm excitation, which agrees with the lower UCL intensities and shorter UCL decay times. The trends observed for the increase of Er concentration were similar, showing lower sensitivities for higher fractions of Er. On the other hand, significant differences were observed when comparing the different UCNP

configurations (ST and IV). Although the ST samples showed the brightest UCL and longest UCL decay times, the highest sensitivities (for both 980 and 808 nm excitation) were accomplished for the IV configurations (**Figure 3D**). Whereas the differences were not that strong for 980 nm excitation, they were significant when 808 nm excitation was used. These results show the importance of donor-acceptor distance within FRET assays because the IV UCNPs have emitting shells that are closer to the dye acceptors compared to the emitting cores in the case of ST UCNPs. Also, several UCNPs within the same configuration showed quite obvious differences between 980 and 808 nm excitation, e.g., IV05, IV10, ST02, IV02-C, and IV02-S1 (compare orange and blue bars in **Figure 3D**), that cannot be simply explained by the differences in the UCNPs. The slightly different sizes of core and shells within the same configurations (cf. **Table S1**) and the competition between FRET efficiency and surface quenching make intuitive estimations even more complicated. Clearly, a sophisticated model that can quantitatively explain and predict the differences in assay sensitivity would be extremely helpful for the design of FRET-optimized UCNPs.

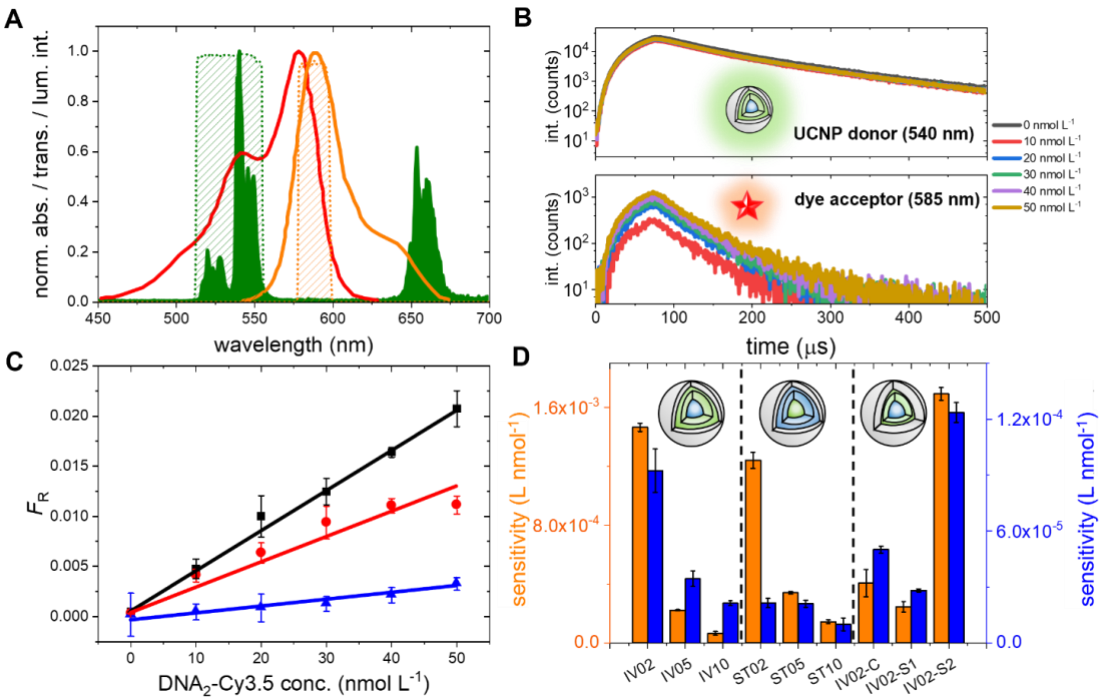

Figure 3. A: Absorption (red) and emission (orange) spectra of Cy3.5 and UCL spectrum of UCNPs (green). The shaded spectra in the background present the spectral bandwidths (filter transmission) of the UCNP (green) and Cy3.5 (orange) luminescence detection channels. **B:** Luminescence decays of UCNP and Cy3.5 at different concentrations of DNA_2-Cy3.5 for the UCNP@PSS-DNA_1-DNA_2-Cy3.5 FRET assay using IV02 as UCNP. **C:** Assay calibration curves and linear fits for the FRET assays using IV02 (black), IV05 (red), and IV10 (blue) UCNPs and 980 nm excitation. **D:** Sensitivities for FRET assays with all nine different UCNPs with 980 nm (orange) and 808 nm (blue) excitation. Error bars in C and D were determined from triplicate measurements.

Modeling of experimental data. For both excitation wavelengths, modeled UCL decay times (**Figure 4A/B**) and sensitivities (**Figure 4C/D**) corresponded very well to the experimental values with only minor deviations from strict correlation (diagonal lines in **Figures 4A-D**) for almost all samples. An interesting feature of the model is the determination of the Förster distance and the luminescence quantum yield of the Er donors. Modeling the experimental data resulted in a Förster distance of R_0 = 3.45 nm, which corresponded to an Er donor luminescence quantum yield of 1%, when using the spectral overlap of Er donor emission and dye acceptor absorption (J = $8.98 \cdot 10^{15}$ $M^{-1}cm^{-1}nm^4$), a dynamically averaged orientation factor (κ^2 = 2/3), and the refractive index of water (n = 1.33). Considering this R_0, the closest FRET distance of ~3 nm (PSS coating and C_3 spacer) provided a FRET efficiency of ~70%, which decreased to ~1% for 7.4 nm Er-dye distance. Although the excitation power dependence of UCL can in principle be included in the model by adding an absorption cross-section term for Nd or Yb, we did not use such additional terms because the excitation power density (as well as the excitation time, UCNP concentration, and sample volume) was kept constant (211.4 $mW \cdot cm^{-2}$) for all experiments. The model was also used to determine the contributions of the different processes to the total UCL kinetic constant $k_{\mathrm{tot}}^{\mathrm{Er}}$ (**Figure 4E/F**), allowing for a quantitative analysis of the trends shown in the UCL decay curves (**Supporting Figure S7)** by correlating the longer or shorter decay times to the dominant physical processes in each UCNP, i.e., environmental quenching ($k_{\mathrm{Q}}^{\mathrm{Er}}$, black bars in **Figure 4E/F**), Er-Er CR ($k_{\mathrm{CR}}^{\mathrm{ErEr}}$, red bars in **Figure 4E/F**), and Er-Nd CR ($k_{\mathrm{CR}}^{\mathrm{ErNd}}$, blue bars in **Figure 4E/F**). When looking at the absolute values of the rate constants for all UCNPs and both excitation wavelengths, environmental quenching has the highest contribution, followed by Er-Nd CR and Er-Er CR. This relatively strong environmental quenching (even for the thickest shell) clarified the importance of a protective shell and confirmed previous findings that suggested a shell thickness of at least 2 nm to efficiently suppress surface quenching.[52] In the most cases, the importance of environmental quenching was significantly higher for 808 nm excitation, whereas Er-Nd CR and Er-Er CR were less important. A possible reason may be the higher amount of necessary ET steps from the initial Nd sensitizer to the final Er activator, which provides more possibilities of quenching via the UCNP surface.

Comparing the relative contributions of each quenching mechanism in reference to the different UCNP configurations (i.e., direct comparison of the heights of the different bars in **Figure 4E/F**) provides additional

interesting information. For example, at 980 nm excitation (where Nd is not excited), the Er-Nd CR was significantly more important for highly Er doped ST compared to IV UCNPs. This was probably caused by the higher number of Er ions in close proximity to Nd ions for CR in ST configurations. For the IV UCNPs, environmental quenching and Er-Er CR were more important for UCNPs with higher Er fractions. In this case, there were not only less Er-Nd interactions (and therefore relatively more Er-Er interactions), but the emitting shell was also closer to the outer environment. For 808 nm excitation, Er-Nd CR was important for almost all ST and IV UCNPs with higher Er fractions. In these cases, Nd was directly excited and transfered its energy to Er, preferentially via Yb to avoid CR. With higher Er concentrations, direct excitation of Er via Nd and Er-Nd CR became more likely, leading to an increasing importance of the Er-Nd CR process. These findings confirm that Er doping concentrations should not be too high to avoid UCL quenching via CR.

Another interesting result that strikes the eye is the importance of environmental quenching in the IV02-S1 UCNPs. These UCNPs had a thick emitting shell without protective shell, which explains that quenching via the UCNP surface was dominant. Surprisingly, changing the C-S1 core-shell volume ratio for the absorbing-core/emitting-shell IV configuration from 70/30 (IV02-C) to 40/60 (IV02-S2), did not result in significant differences for all three contributions (k_Q^{Er}, k_{CR}^{ErEr}, and k_{CR}^{ErNd}) at both 980 and 808 nm excitation. Taking into account that the volume of the emitting S1 shell in IV02-C was only ~16% lower than in IV02-S2, the much larger (~2.7-fold) absorbing core most probably compensated the slightly lower S1 volume and the slightly thinner protective shell (1.2 vs. 1.5 nm).

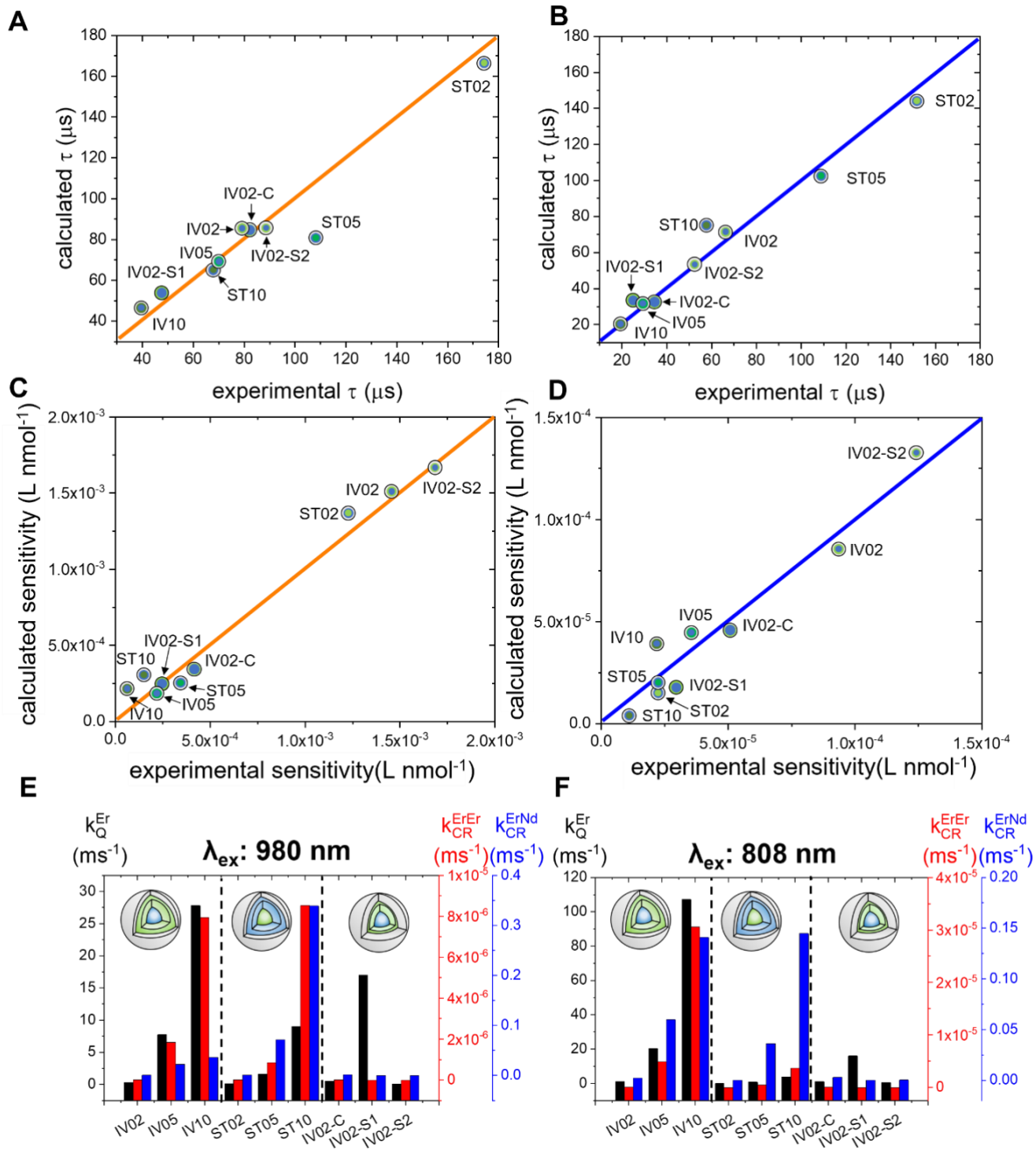

Figure 4. Comparison of calculated and experimental results. Top: Correlation plots of experimental and fitted UCL decay times (τ) at 980 nm (**A**) and 808 nm (**B**) excitation for all the UCNP@PSS-DNA$_1$. Middle: Correlation plots of experimental and fitted DNA$_2$-Cy3.5 hybridization FRET assay sensitivity at 980 nm (**C**) and 808 nm (**D**) excitation. Bottom: Contributions of environmental quenching ($k_{\mathrm{Q}}^{\mathrm{Er}}$, black), Er-Er CR ($k_{\mathrm{CR}}^{\mathrm{ErEr}}$, red), and Er-Nd CR ($k_{\mathrm{CR}}^{\mathrm{ErNd}}$, blue) to overall UCL quenching of the different UCNP@PSS-DNA$_1$ at 980 nm (**E**) and 808 nm (**F**) excitation.

Prediction of Er doping and core-shell-shell size effects on sensitivity. Considering that our analytical model can very well reproduce both the UCL kinetics and the sensitivity of the DNA-hybridization FRET assay, one of the most interesting features is the possibility to predict the FRET-assay sensitivity for arbitrarily designed UCNPs as a function of Er doping, configuration, and section sizes. We first optimized each parameter keeping the others fixed to check the predictivity of the model. Concerning Er concentration (**Figure 5A**), similar trends were found for both configurations (ST and IV) and both excitation wavelengths (980 and 808 nm). A steep sensitivity increase at low doping was followed by a relatively narrow maximum between circa 2 and 3% Er doping and a constant decrease toward higher doping concentrations. The shape of the curve resulted from two opposite contributions. By increasing the concentration of Er, the number of donors in the UCNP-dye FRET pair increased, which led to an increase of k_{FRET}^{c}. On the other hand, with increasing amounts of Er, the different quenching mechanisms within k_{tot}^{Er} (cf. equation 3) also increased (cf. **Figure 4**), thereby reducing the sensitivity. The first contribution was dominant at very low concentrations, whereas the second became prevalent for higher Er content.

Concerning UCNP core radius (R_C, **Figure 5B**), an emitting core (ST) requires a certain size to obtain a sufficient amount of Er donors for FRET. Thus, the sensitivity increased until a maximum was reached at around 4 to 6 nm, after which too many Er ions were too far away from dye acceptors, resulting in decreased sensitivities with larger radii. Whereas the results were very similar for both excitation wavelengths, the opposite configuration with absorbing core and emitting shell (IV) required significantly larger core sizes for reaching maximum sensitivity. As the core contains only absorbing ions (Nd and Yb), increasing radii led to higher absorption cross sections of the UCNPs. However, energy migration to the emitting shell was only efficient until a certain radius between approximately 8 and 11 nm. Owing to the closer distance of Er ions in an emitting shell to acceptors at the surface of the UCNP, the maximum sensitivity in IV-UCNP-containing FRET assays was ~3-fold higher compared to ST-UCNPs. This modeling result also confirms the high FRET efficiencies found for IV-UCNP configurations (but without Nd) in previous studies.[47]

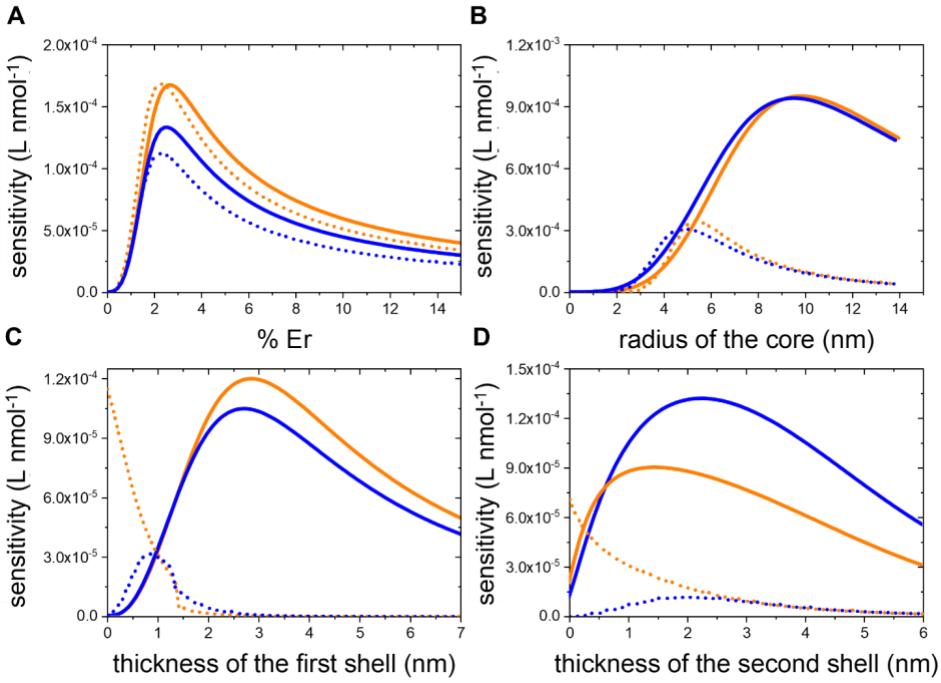

Figure 5: Modeled sensitivity for IV (solid lines) and ST (dotted lines) UCNP configurations at 980 nm (orange) and 808 nm (blue) excitation as a function of **A:** Er doping (R_C = 5 nm, d_{S1} = 1 nm, d_{S2} = 1 nm); **B:** radius of the core (χ_{Er} = 2%, d_{S1} = 1 nm, d_{S2} = 1 nm); **C:** thickness of the first shell (χ_{Er} = 2%, R_C = 5 nm, d_{S2} = 1 nm); and **D:** thickness of the protective shell (χ_{Er} = 2 %, R_C = 5 nm, d_{S1} = 1 nm).

Significantly different results were found for the shell thicknesses concerning both the different configurations and the different excitation wavelengths. Regarding the first shell (**Figure 5C**), the ST configuration and 980 nm excitation led to the highest sensitivity without any shell (0 nm thickness) because Yb ions are present in both the absorbing shell and the emitting core and Nd cannot absorb 980 nm light. Therefore, this first shell is not necessary for absorption and thicker shells decrease the sensitivity because the increasing Er donor to dye acceptor distance is prevalent over the additional absorption of Yb in the shell. For 808 nm excitation, Nd ions are necessary, and a maximum sensitivity was reached at around 1 nm shell thickness. For thicker shells the Er-to-dye distance increase was again outweighing the higher amount of absorbing Nd ions. We note that the slight discontinuity in the ST configuration curves (steep decrease around 1.4 nm) was caused by computational features. For the IV configuration, in which the first shell contained the Er donors, similar trends were found for both excitation wavelengths. Again, the maxima were reached when the beneficial increase of donors was outbalanced by the amount of Er ions that were too distant from the dye acceptors for efficient FRET and by the reduction of ET efficiency from the absorbing core to the emitting shell. The maxima were located between 2 and

3 nm and their sensitivities were similar to the maximum for 980 nm excitation and ST configuration (without shell) but approximately 3 to 4 times higher than 808 nm excitation and ST configuration (with a ~1 nm shell).

Regarding the second shell (**Figure 5D**), the ST configuration and 980 nm excitation also resulted in the highest sensitivity without any shell (0 nm thickness) because the first absorbing shell already serves as protective shell. The shallower decrease of the curve with increasing thickness compared to shell 1 (cf. **Figure 5C**) was most probably caused by the additional Yb sensitizers in shell 1, which contributed to Er sensitization and were protected from quenching with increasing shell 2 thickness. Because Nd was present only in shell 1, excitation at 808 nm required to protect shell 1 from environmental quenching and a maximum sensitivity was attained at a shell 2 thickness between circa 1.5 and 3 nm, after which the sensitivity decreased again. For a thin protective shell 2 the FRET distance is shorter, but the environmental quenching is more important, whereas for a thick protective shell 2 the quenching is prevented but FRET becomes inefficient. For the IV configuration, similar trends appeared for both excitation wavelengths, i.e., a relatively sharp increase of sensitivity with shell thickness, followed by a relatively broad maximum between circa 1.5 and 3.5 nm for 980 nm excitation and 0.5 and 2.5 nm for 808 nm excitation and decreasing sensitivity for thicker shells due to decreasing FRET efficiencies. Thicker protective shells were required for 808 nm excitation because the additional ET made the UC process more prone to quenching. Maximum sensitivities were significantly higher for IV UNCP systems and the highest for 808 nm excitation.

Overall, the dependence of the FRET assay sensitivity on the different UCNP parameters revealed that donor-acceptor distance plays the paramount role and that some basic requirements concerning donor concentration and protection against luminescence quenching must be met. As expected from FRET theory and the Förster distance of $R_0 = 3.45$ nm, Er-to-dye distances beyond 7 nm cannot significantly contribute to FRET. Within the ST configuration, this FRET distance constraint is clearly expressed by a relatively small emitting core (**Figure 5B**) and relatively thin shells (**Figures 5C** and **D**) for sufficient protection against surface quenching. These shells must be a little thicker for 808 nm excitation because Nd sensitizers are present only in shell 1 and must be additionally protected from the environment by shell 2. The IV configuration has distinct advantages because the Er donors can only be found in shell 1 and are therefore closer to the dye acceptors. In this case, the

absorbing core can be relatively large (**Figure 5B**) because it can efficiently transfer the energy to the emitting shell, which can be relatively thin (**Figure 5C**) for the FRET distance advantage while still possessing sufficient volume. Shell 2 must protect the emitting shell but it cannot be too thick because of the FRET distance constraint (**Figure 5D**). One must keep in mind that the single-parameter optimization was performed by fixing all the other parameters and thus, the maxima of the curves in **Figure 5** are not necessarily the optimum values for the individual parameters.

Another interesting possibility of our model is the optimization of a dual-wavelength excitable UCNP for FRET biosensing, i.e., a UCNP that provides the best compromise of sensitivity for excitation at 808 nm and 980 nm. In this way, the same UCNP can be used with 808 nm excitation for samples, in which water absorption and/or sample heating must be avoided and with 980 nm excitation, when water absorption is of minor importance. Also, as the UCL decay times are different for the two excitation wavelengths, such a dual-wavelength excitable UCNP could possibly be used for temporal multiplexing, in which different biological targets are distinguished via their UCL decay times.[10] For a prediction of such a dual-wavelength optimized sensitivity, the two sensitivities (980 nm and 808 nm) from **Figure 5** can be simply combined using their geometrical average ($\bar{x} = \sqrt[n]{\prod x_i}$). Especially for the shell thicknesses, which showed significantly different sensitivity trends at 980 or 808 nm excitation, such an averaging can be quite useful to find optimal dual-wavelength excitation conditions (**Supporting Figure S9**).

Determination of the optimal 808/980 nm photoactivatable FRET-UCNP configuration. As mentioned above, the most powerful feature of a model would be the prediction of an optimal UCNP without synthesizing, characterizing, and evaluating many UCNPs. Considering that the entire experimental approach would not only require the production of many different UCNPs but also UCNP-DNA functionalization, dye-DNA production, and FRET assays, determination of a global sensitivity maximum from a combined analysis of Er doping, core radius, and shell thicknesses via a straightforward analytical model can save enormous amounts of time, effort, and chemical and biological components. Such a global analysis would also overcome the limitations of UCNP optimization when only one parameter is varied while the others are fixed (vide supra). Our model can provide this predictive power by finding the maximum sensitivity as a function of χ_{Er}, R_C, d_{S1}, and d_{S2} at the same time to quantitatively identifying the optimal characteristics of the system for FRET biosensing. The results

observed at each excitation wavelength for IV and ST configurations are reported in **Table 1**. As found for the optimization of each individual parameter (**Figure 5**), a general trend was a higher sensitivity for the IV configuration and 980 nm excitation. However, the global maxima for both configurations (IV and ST) and both excitation wavelengths (980 nm, 808 nm, and combined) were significantly higher than any of the maxima found for the individual parameter optimization (compare **Table 1** to **Figure 5** and **Supporting Figure S9**). Using the global optimization, even the weakest system (ST and 808 nm excitation) can reach a sensitivity similar to the strongest system (IV and 980 nm excitation) for individual optimization (7.8×10^{-4} L nmol^{-1} in **Table 1** compared to 9.5×10^{-4} L nmol^{-1} in **Figure 5B**), which exemplifies the benefit of globally optimized modelling not only for saving time and money but also for improving assay sensitivity. Interestingly, the modelling results showed that IV requires slightly higher Er doping and larger core sizes but also that different excitation wavelengths can lead to very different optimal UCNP parameters depending on the configuration. The optimum shell thicknesses in both configurations (IV and ST) for 808 nm excitation are very similar, whereas they are very different for 980 nm excitation. These findings confirm that it is important to consider all energy transfer paths from the initial excitation to the final emission. Our results also demonstrate the possible employability of our model as a guideline for the design and optimization of complex UCNP nanoarchitectures. Instead of the slow and iterative work of synthesis, functionalization, and characterization of several UCNPs, the procedure can be performed for a limited selection of representative configurations, the results of their characterizations can be analyzed by our model, and a global sensitivity maximum can be rapidly determined.

Table 1. Optimal UCNP parameters (atomic % of Er (χ_{Er}), core radius (Rc), first shell thickness (d_{S1}), and second shell thickness (d_{S2}) for maximum sensitivity in the UCNP@PSS-DNA$_1$-DNA$_2$-Cy3.5 FRET assay.

	IV configuration			**ST configuration**		
	λ_{ex} = 980 nm	λ_{ex} = 808 nm	Both λ_{ex}	λ_{ex} = 980 nm	λ_{ex} = 808 nm	Both λ_{ex}
χ_{Er}	2.72 %	2.85 %	2.62 %	2.11 %	2.24 %	2.13 %
R_C [nm]	8.68	9.16	8.21	5.83	4.89	6.31
d_{S1} [nm]	1.73	1.10	1.72	0.31	1.11	0.65
d_{S2} [nm]	0.44	0.50	0.21	0.07	0.34	0.36
Sensitivity* [L nmol^{-1}]	4.1×10^{-3}	2.2×10^{-3}	**980:** 4.0×10^{-3} **808:** 2.7×10^{-3}	1.8×10^{-3}	7.8×10^{-4}	**980:** 9.0×10^{-4} **808:** 8.0×10^{-4}

* Due to the brute force algorithm of the model, which saves calculation time but sacrifices resolution in finding a maximum value, the sensitivities have an estimated error of 20%.

CONCLUSIONS

FRET from UCNPs to dyes is a very promising approach to designing highly sensitive assays for the quantification of DNA or RNA. However, it is very difficult to predict the ideal properties of a UCNP for accomplishing the best FRET assay performance because over an extended time period of several hundreds of microseconds many different energy transfer steps occur between the initial excitation of the sensitizer ions, the energy transfer from the activator ions to the FRET acceptors, and the final emission of the FRET acceptors. Moreover, UCNPs can be fabricated with different cores and shells, all of which can have different sizes and contain different lanthanoid ions at different doping ratios. These configurations do not only influence the UCL but also the FRET efficiencies because of different donor-acceptor ratios and distances. The complicated and correlated interactions make it almost impossible to experimentally determine the ideal UCNP for FRET assays because it would require the preparation, characterization, and analytical evaluation of a myriad of different configurations.

To overcome these limitations, we developed a fully analytical model that takes into account several energy transfer pathways, core and shell sizes, and lanthanoid ion doping ratios to determine the optimal UCNP configuration for accomplishing the best analytical sensitivity for DNA hybridization assays by rapid calculation. We tested the model using nine different core-shell-shell UCNPs containing Nd and Yb sensitizers and Er activators at different doping ratios. By fitting the experimental results (FRET-quenched UCL and FRET-sensitized dye fluorescence), the model could very precisely reproduce the DNA hybridization assay sensitivities for both Nd (808 nm) and Yb (980 nm) excitation and also predict the best configuration for UCNP that can be used for DNA FRET assays using both excitation wavelengths. Most importantly, combination of the experimental data and the model was used to determine the optimal UCNP configurations leading to the best assay sensitivities, which were significantly higher than those determined for our nine experimentally produced UCNPs. This result demonstrates that only a small, selected number of synthesized UCNP configurations and FRET experiments is necessary to screen the entire combinatorial library of UCNP configurations with our model to determine the "perfect" UCNP for FRET assay sensitivity within a few minutes. The amounts of time, experimental effort, and

chemical and biological products that can be saved by this simple approach of selecting a few experimental configurations and modeling all the others are extremely important. In addition, the sensitivity of an assay can be significantly improved. It is important to note that our approach aims at optimizing UCNPs and, in this particular study, UCNP design for analytical sensitivity (slope of the assay calibration curve) in FRET DNA hybridization assays. The performance of every FRET biosensor or bioassay depends on many different parameters, including the diagnostic or analytical application, the target to be detected, the target recognition molecules and principle, the environment, the sample type and volume, the experimental conditions and equipment, the acceptor properties, and the background or noise signal. Thus, comparison of FRET biosensing performance between different FRET probes (using UCNPs or any other fluorophores) is only meaningful for a specific target, application, and experimental condition. In principle, our model is not limited to the proposed UCNP doping ratios and architecture and can be extended to analyze and optimize UCL and FRET properties for other complex UCNP architectures and ion combinations and to other analytical performance parameters, such as limit of detection or dynamic range. For example, it would be interesting to investigate the doping ratio of Nd, which was kept constant in our study, to better understand the influence of Nd-Nd cross-relaxation on assay performance. The model ~~It~~ can also be applied to different FRET assays, including sandwich immunoassays and protein-protein interactions or FRET imaging applications to become an important tool toward translating UCNP-based FRET into highly sensitive biosensing and bioimaging ranging from bioanalytical research to clinical diagnostics.

MATERIALS AND METHODS

Chemicals. Yttrium (III) oxide (Y_2O_3, 99.9%), ytterbium (III) oxide (Yb_2O_3, 99.9%), neodymium (III) oxide (Nd_2O_3, 99.9%), and erbium (III) oxide (Er_2O_3, 99.99%) were purchased from Alfa Aesar. Hydrochloric acid (HCl, 37%), sodium trifluoroacetate (NaTFA, 98%), ammonium fluoride (NH_4F, 98%), sodium oleate (NaOA, 97%), 1-octadecene (ODE, 90%), oleic acid (OA, 90%), 2,4,6-trichloro-1,3,5-triazine (TCT), oleylamine (OM, 97%), ethanol (EtOH, 99.8%), N,N-dimethylformamide (DMF), toluene (99.9%), n-hexane (99.9%), cyclohexane (99.9%), nitrosonium tetrafluoroborate ($NOBF_4$, 69.9-78.8 %), poly-sodium 4-styrenesulfonate (PSS, M_w ~ 70.000, 99%), trifluoroacetic acid (TFA, 99%), and HEPES buffer were purchased from Sigma-Aldrich. DNA oligo strands were obtained from Eurogentec (**Table 2**) and used as received. All chemicals were used as received without further purifications. Highly pure water (Millipore) of resistivity greater than 18.0 MΩ cm was used in all experiments.

Table 2: Label and nucleic acid sequences of the single-stranded DNA (ssDNA) used for the UCNP functionalization and FRET assay. Orientation adapted to direction of hybridization.

Label	Nucleic acid sequence
DNA_1	(5') H_2N-CCC-GCTATATGAATTCCAG (3')
DNA_2-Cy3.5	(3') Cy3.5-CGATATACTTAAGGTC (5')

Synthesis of oleate-coated β-$NaYF_4$:Yb^{3+}(20 mol%), Nd^{3+}(20 mol %) and β-$NaYF_4$:Yb^{3+}(20 mol%), Er^{3+}(2, 5, 10 mol %) cores. Both cores were prepared by slightly modifying a previous procedure.[71] Briefly, $LnCl_3$ precursors were prepared starting from the respective Ln_2O_3. Depending on the desired core, proper amounts of Ln_2O_3 (for a total of 1.00 mmol of Ln^{3+}) were dissolved in hydrochloric acid (4.2 mL, 1.7 mol·L^{-1}). The mol % of each Ln^{3+} ions in the core are summarized in **Table S1**. The obtained dried $LnCl_3$ precursors were first dissolved under vacuum and magnetic stirring in 6 mL of OA and 15 mL of ODE and then after the addition and complete dissolution of NaOA (2.5 mmol) and NH_4F (4.0 mmol) were left to react under Ar flow at 310 °C for 30 min. After this time the solution was cooled down to room temperature under argon flow and the nanoparticles were precipitated with ethanol and collected by centrifugation (2147 RCF for 15 min). The resulting white pellet was further washed four times with a mixture of hexane/ethanol (1/3) and isolated by centrifugation (2147 RCF, 15 min). Finally, the white pellet was redispersed in ODE. A small amount of powder was dried for XRD and TGA analysis.

Synthesis of oleate-coated α-$NaYF_4$ sacrificial nanoparticles (s-YNPs). α-$NaYF_4$ sacrificial NPs were synthesized via the co-thermolysis of NaTFA and $Y(TFA)_3$ using a previously reported procedure.[71] Briefly, The $Y(TFA)_3$ precursor was prepared by refluxing Y_2O_3 (1 mmol) in 10 mL of 1:1mixture of TFA and ultrapure water under stirring at 80°C overnight. Hereafter, at the obtained dried solid 2 mmol of NaTFA was added along with 6 mL of OA, 6 mL of OM, and 10 mL of ODE under argon flow. The mixture was heated to 125 °C under vacuum and vigorous stirring for several minutes and after at 290 °C under argon flow, where it was kept for 45 min. The light-yellow turbid solution obtained was cooled to room temperature and the s-YNPs were precipitated by adding ethanol and isolated by centrifugation (2147 RCF, 15 min). The obtained precipitate was washed twice as reported for core UCNPs. Finally, the nanoparticles were dispersed in ODE (0.30 mmol·L^{-1}).

Synthesis of oleate-coated α-$NaYF_4$:Yb(20 mol%), Nd(20 mol%) sacrificial nanoparticles (s-NdNPs – see Figure S10 for characterization). The synthesis of α-$NaYF_4$:Yb^{3+}, Nd^{3+} was carried out exactly as reported for undoped α-$NaYF_4$ sacrificial nanoparticles, starting from Y_2O_3 Yb_2O_3, and Nd_2O_3. Finally, the obtained nanoparticles were centrifuged and washed as above and dispersed in ODE (0.3 mmol·L^{-1}).

Synthesis of oleate-coated β-$NaYF_4$:Yb^{3+}(20 mol%), Nd^{3+}(20 mol%)/$NaYF_4$:Yb^{3+}(20 mol%), Er^{3+}(2, 5 and 10 mol%)/$NaYF_4$ core-shell-shell nanoparticles (IV02, IV05, IV10, IV02-C, IV02-S1, IV2-S2). $LnCl_3$ precursors for the emitting shell were prepared as previously described for β-cores. In this case after the addition and complete dissolution of NaOA (2.5 mmol) and NH_4F (4.0 mmol) 2 mL of ODE containing the previously synthesized absorbing β-$NaYF_4$:Yb^{3+}(20), Nd^{3+}(20) core (the mols of core introduced depend on the specific systems) were injected in the reaction flask and the solution was first heated up to 120°C in vacuum and then to 310°C under Ar flow where was kept for 30 minutes after reaching this temperature. At this point first 1.0 mL of reaction mixture was collected (core-shell sample) and immediately after undoped sacrificial nanoparticles (s-YNPs) (0.30 mmol in 1 mL of ODE) were injected. Depending on the desired thickness of the inert shell the injection was repeated after 15 minutes (for IV02-S2). Then, the solution was cooled down to room temperature under argon flow and the NPs were precipitated from the solution with ethanol and collected by centrifugation

(2147 RCF for 15 min) and washed several times as reported for core NPs. Finally, the white pellet was stored in ethanol. A small amount of powder was dried for XRD and TGA analysis.

Synthesis of oleate-coated β-$NaYF_4$:Yb^{3+}(20 mol%), Er^{3+}(2, 5, 10 mol%)/$NaYF_4$:Yb^{3+}(20 mol%), Nd^{3+}(20 mol%)/$NaYF_4$ core-shell-shell nanoparticles (ST2, ST5, ST10). The synthesis of core nanoparticles was carried out as described above. At the end of the core synthesis, i.e., after keeping the reaction mixture at 310 °C for 30 min about 1.0 mL of reaction mixture was collected from the flask (core sample) and immediately after s-NdNPs (0.30 mmol in 1.0 mL of ODE) were injected by a syringe in a single shot into the reaction mixture and the mixture was ripened for 15 min at 310 °C. After ripening of the first shell, again 1.0 mL of the reaction mixture was collected and immediately after sacrificial undoped s-YNPs (0.30 mmol in 1.0 mL of ODE) were injected. The mixture was ripened for another 15 min to yield the standard core-shell-shell NPs (ST2, ST5, ST10). All the prepared samples are summarized in **Table S1**. Then, the solution was cooled down to room temperature under argon flow and the NPs were precipitated from the solution with ethanol and collected by centrifugation (2147 RCF for 15 min) and washed several times as reported for core NPs. Finally, the white pellet was stored in ethanol. A small amount of powder was dried for XRD and TGA analysis.

Exchange of the oleate ligand with BF_4^- (UCNP@BF_4). All the as prepared oleate-coated core-shell-shell UCNPs (UCNP@OA) were treated with $NOBF_4$ to remove the oleate ligands following a previously reported method.[71] In a 15 mL centrifuge tube 5 mL of UCNP@OA dispersed in cyclohexane (5 mg·mL^{-1}) were mixed to 5 mL of 0.01 mol·mL^{-1} $NOBF_4$ in DMF. After 10 min a precipitate appeared and then was centrifuged (7000 rcf, 5 min). The supernatant was decanted, and the pellet was redispersed in DMF to have a 5 mg·mL^{-1} dispersion, an amount of five times the volume of DMF of toluene/cyclohexane (1:1) solution was added to precipitate the UCNPs. The procedure was repeated three times and then the pellet was dispersed in DMF (20 mg·mL^{-1})

Functionalization of core-shell-shell UCNPs with polystyrene sulphonate (UCNP@PSS). The BF_4^- was substituted with PSS by ligand exchange according a previously optimized procedure.[72] Then, 5 mL of UCNP@BF_4 in DMF (20 mg·mL^{-1}) were mixed with 1.7 mL of 30 $\%_{w/w}$ PSS in ultrapure water under vigorous stirring and kept at 60°C for 24 hours. After that, the dispersion was centrifuged (10000 rcf for 30 min). The supernatant was removed, and the pellet was redispersed in 10 mL of ultrapure water and collected by centrifugation (10000 rcf for 30 min). This step was repeated for three times. Then the UCNP@PSS were redispersed in DMF (10 mg/mL). The procedure was applied to all the core-shell- shell NPs synthesized.

Bioconjugation of UCNP@PSS with amino-modified single stranded DNA (UCNP@PSS-DNA_1). The bioconjugation of all the UCNP@PSS with the amino-modified ssDNA (DNA_1) was performed according a previously reported procedure.[9] A 10 mg/mL solution of TCT in DMF (solution A) was stirred at 600 rpm at 25°C for one hour. After that, 200 µL of solution A were mixed with 600 µL of 10 mg/mL UCNP@PSS dispersion and 2 mL of DCM, the dispersion was left under magnetic stirring and argon atmosphere for one hour. Then, 100 µL of 100 µmol·L^{-1} solution of DNA_1 in ultrapure water were added and the dispersion was stirred overnight under Argon atmosphere. The day after the dispersion was transferred in a centrifuge tube and washed three times by centrifugation and redispersion in ultrapure water at 10000 rcf for 30 minutes. Finally, the samples were redispersed in ultrapure water, obtaining a 1 mg·mL^{-1} dispersion.

Conjugation of UCNP@PSS-DNA_1 with cyanine-modified single stranded DNA (UCNP@PSS-DNA_1-DNA_2-Cy3.5). For each NPs architecture, the dispersions used for FRET experiments were prepared adding a variable volume of DNA_2-Cy3.5 stock solution (concentration 1 µmol·L^{-1}) (final concentrations 0, 1, 5, 10, 50, 100 nmol·L^{-1}) to the same volume of UCNP@PSS-DNA_1 (initial concentration 20 mg/mL, final concentration 1 mg/mL) and diluting with HEPES to a final volume of 200 µL. Before the FRET measurements, the obtained dispersions were magnetically stirred at 600 rcf for 30 min at 35°C.

Transmission Electron Microscopy (TEM). TEM grids were prepared by drop-casting of oleate-capped UCNPs dispersion in toluene (1 mg mL^{-1}) onto 400-mesh carbon-coated Cu grids, followed by air-drying. TEM images were taken on a FEI Tecnai G2 operating at 100 kV, equipped with an Olympus Veleta camera. The Fiji ImageJ software was used to determine the UCNPs sizes, which were obtained as the average diameter of 250 individual NPs. Each intermediate of the core–shell-shell samples were analyzed to determine the shell thickness.

Powder X-ray Diffraction (PXRD). PXRD measurements were carried out with a Bruker D8 Advance diffractometer using Cu Kα radiation (λ = 1.5406 Å) at a voltage of 40 kV and current of 40 mA. PXRD patterns were collected for 2θ = 10–70°, with a step size of 0.03° and a counting time of 10 s per step. The crystalline phases were identified by the search-match method using the JCPDS database. The crystallographic files for cubic and hexagonal $NaYF_4$ were found on Crystallography Open Database[74] with database code 1517672[75] and 1517676[76], respectively. The Rietveld refinement of the structures was performed using diffract.TOPAS software by Bruker. TOPAS is a profile fitting-based software for quantitative phase analysis, microstructure analysis and crystal structure analysis.

Thermal Gravimetric Analysis (TGA - Supporting Figure S11). Selected samples (IV02@OA, and IV02@PSS) were analyzed with TGA to analyze the coatings via monitoring of the mass loss. Moreover, the TGA analysis of sacrificial NPs (sNPs) was useful to evaluate the amount to be injected in the synthesis of ST core-shell-shell NPs (0.30 mmol in 1.0 mL of ODE refers to inorganic mass (without oleate ligands)).TGA was carried out using the SDT 2960 Simultaneous DSC-TGA system (TA Instruments). Thermograms were collected from RT to 700 °C at 10 °C min^{-1} heating rates under nitrogen flow.

Energy Dispersive X-Ray (EDX - Supporting Figure S12) analysis. The localization of the different lanthanoid ions within the UCNPs, IV02 UCNPs was investigated by EDX on a high-resolution TEM instrument (Talos F200S - Thermofisher Scientific) operating at 200 kV. Elemental maps were obtained considering the $K\alpha_1$ and $K\alpha_2$ lines for Y, and $L\alpha_1$ and $L\alpha_2$ lines for Yb, Nd, and Er.

UCL measurements. Steady-state emission spectra were measured on FLS1000 photoluminescent spectrometer (Edinburgh Instruments) equipped with a 2 W 980 nm and 808 nm lasers (Changchun New Industries). Samples had a concentration of 1 mg/mL and were measured in 10 mm quartz cuvettes in the 350-750 nm range with a power density of 60 $W \cdot cm^{-2}$, an emission slit width of 1 nm and a step size of 0.5 nm.

UCL time-resolved measurements and FRET experiments. Time-resolved measurements of the UCNP@OA were performed FLS1000 photoluminescent spectrometer (Edinburgh Instruments) equipped with a 2 W 980 nm and 808 nm lasers (Changchun New Industries) and a PM-1 laser modulation box (Edinburgh Instruments) to control the temporal parameters of the excitation pulse. Samples had a concentration of 1 mg/mL and were measured in 10 mm quartz cuvettes at 410 (blue), 540 (green), 660 nm (red) with 10 nm bandwidth and a power density of 211.4 $mW \cdot cm^{-2}$.

Time-resolved measurements of UCNP@PSS-DNA_1 were performed using a fluorescence plate reader (Edinburgh Instruments) equipped with 2 W 980 nm and 808 nm (Changchun New Industries) and a PM-1 laser modulation box (Edinburgh Instruments) to control the temporal parameters of the excitation pulse. Excitation and emission were separated using a 900 nm dichroic mirror (Edmund Optics) for 980 nm excitation and an 800 nm dichroic mirror (Edmund Optics) for 808 nm excitation. The signals were measured with a photomultiplier tube (PMT) by using 540/56 nm bandpass filter (Semrock) for the UCNP green emission. 150 µL of UCNP@PSS-DNA_1 dispersions in HEPES were pipetted into 96-well glass-coated microplates (Thermo Fisher Scientific). The resulting curves were fitted with single exponential fitting function $y = y_0 + Ae^{-\frac{t}{\tau}}$.

For FRET experiments, the signals were measured using a fluorescence plate reader (Edinburgh Instruments) with a photomultiplier tube (PMT) by using 540/56 nm and 585/15 nm bandpass filters (Semrock) for the UCNP green emission and Cy3.5 emission, respectively. 150 µL of UCNP@PSS-DNA_1-DNA_2-Cy3.5 dispersions in HEPES were pipetted into 96-well glass-coated microplates (Thermo Fisher Scientific). All the dispersions contain 1 $mg \cdot mL^{-1}$ of UCNP@PSS-DNA_1 and variable concentration of DNA_2-Cy3.5 (0, 1, 5, 10, 50, 100 $nmol \cdot L^{-1}$). The measurements were performed with a power density of 16.2 $mW \cdot cm^{-1}$ per pulse and a repetition rate of 200 Hz. All measurements were done in triplicates.

ASSOCIATED CONTENT

Supporting Information

The Supporting Information is available free of charge at ….

Model derivation, TEM, PXRD and Rietveld, Steady-state UCL, Time-resolved UCL (980 nm excitation), Time-resolved UCL (808 nm excitation), UCL decay times of UCNPs exited at 980 nm or 808 nm, Assay calibration curves, Geometrical average of the sensitivities predicted at 980 and 808 nm, Characterization of sacrificial UCNPs, TGA, EDX.

ACKNOWLEDGMENTS

This work was financed by Université Franco-Italienne (UFI, PhD fellowship of Federico Pini), the European Commission (Marie Skłodowska-Curie grant 794410), the Brain Pool program funded by the Ministry of Science and ICT through the National Research Foundation of Korea (2021H1D3A2A0204958912), Seoul National University, Université Rouen Normandie, INSA Rouen Normandie, Centre National de la Recherche Scientifique, the European Regional Development Fund, Labex SynOrg (ANR-11-LABX-0029), Carnot Institute I2C, XL-Chem graduate school (ANR-18-EURE-0020 XL CHEM), Région Normandie, the program of scientific cooperation CNR/CAS 2019-202, Istituto di Chimica della Materia Condensata e Tecnologie per l'Energia, Consiglio Nazionale delle Ricerche, Dipartimento di Scienze Chimiche, Università di Padova. PXRD and fluorescence measurements were performed with a Bruker AXS D8 ADVANCE Plus diffractometer and Edinburgh FLS100 UV/Vis/NIR photoluminescence spectrometer, respectively, at the PanLab department facility, founded by the MIUR-"Dipartimenti di Eccellenza" grant NExuS. Dr. F. Boldrin and Dr. F. Caicci (Dipartimento di Biologia, Universirà di Padova) and G. Ischia (Dipartimento di Ingegneria Industriale, Università di Trento) are acknowledged for producing TEM images and EDX maps.

REFERENCES

(1) Auzel, F. Upconversion and Anti-Stokes Processes with f and d Ions in Solids. *Chem. Rev.* **2004**, *104* (1), 139–174. https://doi.org/10.1021/cr020357g.

(2) Wiesholler, L. M.; Frenzel, F.; Grauel, B.; Würth, C.; Resch-Genger, U.; Hirsch, T. Yb,Nd,Er-Doped Upconversion Nanoparticles: 980 Nm versus 808 Nm Excitation. *Nanoscale* **2019**, *11* (28), 13440–13449. https://doi.org/10.1039/C9NR03127H.

(3) Tessitore, G.; Mandl, G. A.; Brik, M. G.; Park, W.; Capobianco, J. A. Recent Insights into Upconverting Nanoparticles: Spectroscopy, Modeling, and Routes to Improved Luminescence. *Nanoscale* **2019**, *11* (25), 12015–12029. https://doi.org/10.1039/C9NR02291K.

(4) Gnach, A.; Lipinski, T.; Bednarkiewicz, A.; Rybka, J.; Capobianco, J. A. Upconverting Nanoparticles: Assessing the Toxicity. *Chem. Soc. Rev.* **2015**, *44* (6), 1561–1584. https://doi.org/10.1039/C4CS00177J.
(5) Zhang, D.; Peng, R.; Liu, W.; Donovan, M. J.; Wang, L.; Ismail, I.; Li, J.; Li, J.; Qu, F.; Tan, W. Engineering DNA on the Surface of Upconversion Nanoparticles for Bioanalysis and Therapeutics. *ACS Nano* **2021**, *15* (11), 17257–17274. https://doi.org/10.1021/acsnano.1c08036.
(6) Ansari, A. A.; Thakur, V. K.; Chen, G. Functionalized Upconversion Nanoparticles: New Strategy towards FRET-Based Luminescence Bio-Sensing. *Coord. Chem. Rev.* **2021**, *436*, 213821. https://doi.org/10.1016/j.ccr.2021.213821.
(7) Wang, J.; Sheng, T.; Zhu, X.; Li, Q.; Wu, Y.; Zhang, J.; Liu, J.; Zhang, Y. Spectral Engineering of Lanthanide-Doped Upconversion Nanoparticles and Their Biosensing Applications. *Mater. Chem. Front.* **2021**, *5* (4), 1743–1770. https://doi.org/10.1039/D0QM00910E.
(8) Jin, B.; Li, Z.; Zhao, G.; Ji, J.; Chen, J.; Yang, Y.; Xu, R. Upconversion Fluorescence-Based Paper Disc for Multiplex Point-of-Care Testing in Water Quality Monitoring. *Anal. Chim. Acta* **2021**, 339388. https://doi.org/10.1016/j.aca.2021.339388.
(9) Francés-Soriano, L.; Estebanez, N.; Pérez-Prieto, J.; Hildebrandt, N. DNA-Coated Upconversion Nanoparticles for Sensitive Nucleic Acid FRET Biosensing. *Adv. Funct. Mater.* **2022**, *32* (37), 2201541. https://doi.org/10.1002/adfm.202201541.
(10) Qiu, X.; Xu, J.; Cardoso Dos Santos, M.; Hildebrandt, N. Multiplexed Biosensing and Bioimaging Using Lanthanide-Based Time-Gated Förster Resonance Energy Transfer. *Acc. Chem. Res.* **2022**, *55* (4), 551–564. https://doi.org/10.1021/acs.accounts.1c00691.
(11) Fan, Y.; Zhang, F. A New Generation of NIR-II Probes: Lanthanide-Based Nanocrystals for Bioimaging and Biosensing. *Adv. Opt. Mater.* **2019**, *7* (7), 1801417. https://doi.org/10.1002/adom.201801417.
(12) Chen, T.; Shang, Y.; Zhu, Y.; Hao, S.; Yang, C. Activators Confined Upconversion Nanoprobe with Near-Unity Förster Resonance Energy Transfer Efficiency for Ultrasensitive Detection. *ACS Appl. Mater. Interfaces* **2022**, acsami.2c00604. https://doi.org/10.1021/acsami.2c00604.
(13) Wang, Y.; Song, S.; Zhang, S.; Zhang, H. Stimuli-Responsive Nanotheranostics Based on Lanthanide-Doped Upconversion Nanoparticles for Cancer Imaging and Therapy: Current Advances and Future Challenges. *Nano Today* **2019**, *25*, 38–67. https://doi.org/10.1016/j.nantod.2019.02.007.
(14) Sun, S.-K.; Wang, H.-F.; Yan, X.-P. Engineering Persistent Luminescence Nanoparticles for Biological Applications: From Biosensing/Bioimaging to Theranostics. *Acc. Chem. Res.* **2018**, *51* (5), 1131–1143. https://doi.org/10.1021/acs.accounts.7b00619.
(15) Chen, G.; Qiu, H.; Prasad, P. N.; Chen, X. Upconversion Nanoparticles: Design, Nanochemistry, and Applications in Theranostics. *Chem. Rev.* **2014**, *114* (10), 5161–5214. https://doi.org/10.1021/cr400425h.
(16) Wang, J.; Su, Q.; Lv, Q.; Cai, B.; Xiaohalati, X.; Wang, G.; Wang, Z.; Wang, L. Oxygen-Generating Cyanobacteria Powered by Upconversion-Nanoparticles-Converted Near-Infrared Light for Ischemic Stroke Treatment. *Nano Lett.* **2021**. https://doi.org/10.1021/acs.nanolett.1c00719.
(17) Meijer, M. S.; Talens, V. S.; Hilbers, M. F.; Kieltyka, R. E.; Brouwer, A. M.; Natile, M. M.; Bonnet, S. NIR-Light-Driven Generation of Reactive Oxygen Species Using Ru(II)-Decorated Lipid-Encapsulated Upconverting Nanoparticles. *Langmuir* **2019**, *35* (37), 12079–12090. https://doi.org/10.1021/acs.langmuir.9b01318.
(18) Anderson, R. B.; Smith, S. J.; May, P. S.; Berry, M. T. Revisiting the NIR-to-Visible Upconversion Mechanism in β-NaYF4:Yb3+,Er3+. *J. Phys. Chem. Lett.* **2014**, *5* (1), 36–42. https://doi.org/10.1021/jz402366r.
(19) Arppe, R.; Hyppänen, I.; Perälä, N.; Peltomaa, R.; Kaiser, M.; Würth, C.; Christ, S.; Resch-Genger, U.; Schäferling, M.; Soukka, T. Quenching of the Upconversion Luminescence of NaYF4:Yb3+,Er3+ and NaYF4:Yb3+,Tm3+ Nanophosphors by Water: The Role of the Sensitizer Yb3+ in Non-Radiative Relaxation. *Nanoscale* **2015**, *7* (27), 11746–11757. https://doi.org/10.1039/C5NR02100F.

(20) Frenzel, F.; Würth, C.; Dukhno, O.; Przybilla, F.; Wiesholler, L. M.; Muhr, V.; Hirsch, T.; Mély, Y.; Resch-Genger, U. Multiband Emission from Single β-NaYF4(Yb,Er) Nanoparticles at High Excitation Power Densities and Comparison to Ensemble Studies. *Nano Res.* **2021**, *14*, 4107–4115. https://doi.org/10.1007/s12274-021-3350-y.

(21) Villanueva-Delgado, P.; Kram, K. W. Simulating Energy Transfer and Upconversion in B-NaYF4: Yb3+, Tm3+. *J. Phys. Chem. C* **2015**, *119*, 23648–23657.

(22) Wong, H.-T.; Vetrone, F.; Naccache, R.; Chan, H. L. W.; Hao, J.; Capobianco, J. A. Water Dispersible Ultra-Small Multifunctional KGdF4:Tm3+, Yb3+ Nanoparticles with near-Infrared to near-Infrared Upconversion. *J. Mater. Chem.* **2011**, *21* (41), 16589–16596. https://doi.org/10.1039/C1JM12796A.

(23) Jiang, X.; Cao, C.; Feng, W.; Li, F. Nd3+-Doped LiYF4 Nanocrystals for Bio-Imaging in the Second near-Infrared Window. *J. Mater. Chem. B* **2015**, *4* (1), 87–95. https://doi.org/10.1039/C5TB02023A.

(24) Ma, Q.; Wang, J.; Li, Z.; Lv, X.; Liang, L.; Yuan, Q. Recent Progress in Time-Resolved Biosensing and Bioimaging Based on Lanthanide-Doped Nanoparticles. *Small* **2019**, *15* (32), 1804969. https://doi.org/10.1002/smll.201804969.

(25) Li, Z.; Liang, T.; Wang, Q.; Liu, Z. Strategies for Constructing Upconversion Luminescence Nanoprobes to Improve Signal Contrast. *Small* **2020**, *16* (1), 1905084. https://doi.org/10.1002/smll.201905084.

(26) Matulionyte, M.; Skripka, A.; Ramos-Guerra, A.; Benayas, A.; Vetrone, F. The Coming of Age of Neodymium: Redefining Its Role in Rare Earth Doped Nanoparticles. *Chem. Rev.* **2022**, *123* (1), 515–554. https://doi.org/10.1021/acs.chemrev.2c00419.

(27) Zhang, Y.; Yu, Z.; Li, J.; Ao, Y.; Xue, J.; Zeng, Z.; Yang, X.; Tan, T. T. Y. Ultrasmall-Superbright Neodymium-Upconversion Nanoparticles via Energy Migration Manipulation and Lattice Modification: 808 Nm-Activated Drug Release. *ACS Nano* **2017**, *11* (3), 2846–2857. https://doi.org/10.1021/acsnano.6b07958.

(28) del Rosal, B.; Pérez-Delgado, A.; Misiak, M.; Bednarkiewicz, A.; Vanetsev, A. S.; Orlovskii, Y.; Jovanović, D. J.; Dramićanin, M. D.; Rocha, U.; Upendra Kumar, K.; Jacinto, C.; Navarro, E.; Martín Rodríguez, E.; Pedroni, M.; Speghini, A.; Hirata, G. A.; Martín, I. R.; Jaque, D. Neodymium-Doped Nanoparticles for Infrared Fluorescence Bioimaging: The Role of the Host. *J. Appl. Phys.* **2015**, *118* (14), 143104. https://doi.org/10.1063/1.4932669.

(29) Lin, S.-L.; Chang, C. A. Optimising FRET-Efficiency of Nd3+-Sensitised Upconversion Nanocomposites by Shortening the Emitter–Photosensitizer Distance. *Nanoscale* **2020**, *12* (16), 8742–8749. https://doi.org/10.1039/D0NR01821J.

(30) Agazzi, L.; Wörhoff, K.; Pollnau, M. Energy-Transfer-Upconversion Models, Their Applicability and Breakdown in the Presence of Spectroscopically Distinct Ion Classes: A Case Study in Amorphous Al2O3:Er3+. *J. Phys. Chem. C* **2013**, *117* (13), 6759–6776. https://doi.org/10.1021/jp4011839.

(31) Algar, W. R.; Hildebrandt, N.; Vogel, S. S.; Medintz, I. L. FRET as a Biomolecular Research Tool — Understanding Its Potential While Avoiding Pitfalls. *Nat. Methods* **2019**, *16* (9), 815–829. https://doi.org/10.1038/s41592-019-0530-8.

(32) Medintz, I.; Hildebrandt, N. *FRET - Förster Resonance Energy Transfer : From Theory to Applications*, 1st ed.; Wiley-VCH Verlag GmbH & Co. KGaA, Weinheim, 2014, Vol. 1.

(33) Yao, Y.; Xie, G.; Zhang, X.; Yuan, J.; Hou, Y.; Chen, H. Fast Detection of E. Coli with a Novel Fluorescent Biosensor Based on a FRET System between UCNPs and GO@Fe3O4 in Urine Specimens. *Anal. Methods* **2021**, *13* (19), 2209–2214. https://doi.org/10.1039/D1AY00320H.

(34) Francés-Soriano, L.; Leino, M.; Dos Santos, M. C.; Kovacs, D.; Borbas, K. E.; Söderberg, O.; Hildebrandt, N. *In Situ* Rolling Circle Amplification Förster Resonance Energy Transfer (RCA-FRET) for Washing-Free Real-Time Single-Protein Imaging. *Anal. Chem.* **2021**, *93* (3), 1842–1850. https://doi.org/10.1021/acs.analchem.0c04828.

(35) Liu, G. Advances in the Theoretical Understanding of Photon Upconversion in Rare-Earth Activated Nanophosphors. *Chem. Soc. Rev.* **2015**, *44* (6), 1635–1652. https://doi.org/10.1039/C4CS00187G.

(36) Mattsson, L.; Wegner, K. D.; Hildebrandt, N.; Soukka, T. Upconverting Nanoparticle to Quantum Dot FRET for Homogeneous Double-Nano Biosensors. *RSC Adv.* **2015**, *5* (18), 13270–13277. https://doi.org/10.1039/c5ra00397k.
(37) Francés-Soriano, L.; Peruffo, N.; Natile, M. M.; Hildebrandt, N. Er3+-to-Dye Energy Transfer in DNA-Coated Core and Core/Shell/Shell Upconverting Nanoparticles with 980 Nm and 808 Nm Excitation of Yb3+ and Nd3+. *Analyst* **2020**, *145* (7), 2543–2553. https://doi.org/10.1039/C9AN02532D.
(38) Doughan, S.; Uddayasankar, U.; Peri, A.; Krull, U. J. A Paper-Based Multiplexed Resonance Energy Transfer Nucleic Acid Hybridization Assay Using a Single Form of Upconversion Nanoparticle as Donor and Three Quantum Dots as Acceptors. *Anal. Chim. Acta* **2017**, *962*, 88–96. https://doi.org/10.1016/j.aca.2017.01.025.
(39) Bhuckory, S.; Lahtinen, S.; Höysniemi, N.; Guo, J.; Qiu, X.; Soukka, T.; Hildebrandt, N. Understanding FRET in Upconversion Nanoparticle Nucleic Acid Biosensors. *Nano Lett.* **2023**. https://doi.org/10.1021/acs.nanolett.2c04899.
(40) Rana, S.; Valbuena, G. N.; Curry, E.; Bevan, C. L.; Keun, H. C. MicroRNAs as Biomarkers for Prostate Cancer Prognosis: A Systematic Review and a Systematic Reanalysis of Public Data. *Br. J. Cancer* **2022**, *126* (3), 502–513. https://doi.org/10.1038/s41416-021-01677-3.
(41) Okuda, Y.; Shimura, T.; Iwasaki, H.; Fukusada, S.; Nishigaki, R.; Kitagawa, M.; Katano, T.; Okamoto, Y.; Yamada, T.; Horike, S.; Kataoka, H. Urinary MicroRNA Biomarkers for Detecting the Presence of Esophageal Cancer. *Sci. Rep.* **2021**, *11* (1), 8508. https://doi.org/10.1038/s41598-021-87925-1.
(42) Hanna, J.; Hossain, G. S.; Kocerha, J. The Potential for MicroRNA Therapeutics and Clinical Research. *Front. Genet.* **2019**, *10*, 478. https://doi.org/10.3389/fgene.2019.00478.
(43) Qian, L.; Li, Q.; Baryeh, K.; Qiu, W.; Li, K.; Zhang, J.; Yu, Q.; Xu, D.; Liu, W.; Brand, R. E.; Zhang, X.; Chen, W.; Liu, G. Biosensors for Early Diagnosis of Pancreatic Cancer: A Review. *Transl. Res.* **2019**, *213*, 67–89. https://doi.org/10.1016/j.trsl.2019.08.002.
(44) Zhang, K.; Song, S.; Huang, S.; Yang, L.; Min, Q.; Wu, X.; Lu, F.; Zhu, J.-J. Lighting Up MicroRNA in Living Cells by the Disassembly of Lock-Like DNA-Programmed UCNPs-AuNPs through the Target Cycling Amplification Strategy. *Small* **2018**, *14* (40), 1802292. https://doi.org/10.1002/smll.201802292.
(45) Li, S.; Xu, L.; Ma, W.; Wu, X.; Sun, M.; Kuang, H.; Wang, L.; Kotov, N. A.; Xu, C. Dual-Mode Ultrasensitive Quantification of MicroRNA in Living Cells by Chiroplasmonic Nanopyramids Self-Assembled from Gold and Upconversion Nanoparticles. *J. Am. Chem. Soc.* **2016**, *138* (1), 306–312. https://doi.org/10.1021/jacs.5b10309.
(46) Algar, W. R.; Massey, M.; Rees, K.; Higgins, R.; Krause, K. D.; Darwish, G. H.; Peveler, W. J.; Xiao, Z.; Tsai, H.-Y.; Gupta, R.; Lix, K.; Tran, M. V.; Kim, H. Photoluminescent Nanoparticles for Chemical and Biological Analysis and Imaging. *Chem. Rev.* **2021**, *121* (15), 9243–9358. https://doi.org/10.1021/acs.chemrev.0c01176.
(47) Pilch-Wrobel, A.; Kotulska, A. M.; Lahtinen, S.; Soukka, T.; Bednarkiewicz, A. Engineering the Compositional Architecture of Core-Shell Upconverting Lanthanide-Doped Nanoparticles for Optimal Luminescent Donor in Resonance Energy Transfer: The Effects of Energy Migration and Storage. *Small* **2022**, *18* (18), 2200464. https://doi.org/10.1002/smll.202200464.
(48) Kotulska, A. M.; Pilch-Wróbel, A.; Lahtinen, S.; Soukka, T.; Bednarkiewicz, A. Upconversion FRET Quantitation: The Role of Donor Photoexcitation Mode and Compositional Architecture on the Decay and Intensity Based Responses. *Light Sci. Appl.* **2022**, *11* (1), 256. https://doi.org/10.1038/s41377-022-00946-x.
(49) Jones, C. M. S.; Gakamsky, A.; Marques-Hueso, J. The Upconversion Quantum Yield (UCQY): A Review to Standardize the Measurement Methodology, Improve Comparability, and Define Efficiency Standards. *Sci. Technol. Adv. Mater.* **2021**, *22* (1), 810–848. https://doi.org/10.1080/14686996.2021.1967698.
(50) Chen, B.; Wang, F. Combating Concentration Quenching in Upconversion Nanoparticles. *Acc. Chem. Res.* **2020**, *53* (2), 358–367.

(51) Tian, C.; Chen, X.; Shuibao, Y. Concentration Dependence of Spectroscopic Properties and Energy Transfer Analysis in Nd3+ Doped Bismuth Silicate Glasses. *Solid State Sci.* **2015**, *48*, 171–176. https://doi.org/10.1016/j.solidstatesciences.2015.08.008.
(52) Pini, F.; Francés-Soriano, L.; Peruffo, N.; Barbon, A.; Hildebrandt, N.; Natile, M. M. Spatial and Temporal Resolution of Luminescence Quenching in Small Upconversion Nanocrystals. *ACS Appl. Mater. Interfaces* **2022**, *14* (9), 11883–11894. https://doi.org/10.1021/acsami.1c23498.
(53) Feng, Y.; Li, Z.; Li, Q.; Yuan, J.; Tu, L.; Ning, L.; Zhang, H. Internal OH − Induced Cascade Quenching of Upconversion Luminescence in NaYF 4 :Yb/Er Nanocrystals. *Light Sci. Appl.* **2021**, *10* (1), 105. https://doi.org/10.1038/s41377-021-00550-5.
(54) Hossan, M. Y.; Hor, A.; Luu, Q.; Smith, S. J.; May, P. S.; Berry, M. T. Explaining the Nanoscale Effect in the Upconversion Dynamics of β-NaYF4:Yb3+, Er3+ Core and Core–Shell Nanocrystals. *J. Phys. Chem. C* **2017**, *121* (30), 16592–16606. https://doi.org/10.1021/acs.jpcc.7b04567.
(55) Shi, R.; Brites, C. D. S.; Carlos, L. D. Understanding the Shell Passivation in Ln3+-Doped Luminescent Nanocrystals. *Small Struct.* **2022**, *3* (3), 2100194. https://doi.org/10.1002/sstr.202100194.
(56) Liu, J.; Fu, T.; Shi, C. Upconversion Model for Directly Determining the Microscopic Energy-Transfer Parameters for β-$NaYF_4$:Er^{3+}. *J. Phys. Chem. C* **2020**, *124* (46), 25509–25520. https://doi.org/10.1021/acs.jpcc.0c05305.
(57) Villanueva-Delgado, P.; Krämer, K. W.; Valiente, R.; Jong, M. de; Meijerink, A. Modeling Blue to UV Upconversion in β-NaYF4:Tm3+. *Phys. Chem. Chem. Phys.* **2016**, *18* (39), 27396–27404. https://doi.org/10.1039/C6CP04347J.
(58) Das, A.; Corbella Bagot, C.; Rappeport, E.; Ba Tis, T.; Park, W. Quantitative Modeling and Experimental Verification of Förster Resonant Energy Transfer in Upconversion Nanoparticle Biosensors. *J. Appl. Phys.* **2021**, *130* (2), 023102. https://doi.org/10.1063/5.0053464.
(59) Rabouw, F. T.; Prins, P. T.; Villanueva-Delgado, P.; Castelijns, M.; Geitenbeek, R. G.; Meijerink, A. Quenching Pathways in NaYF4:Er3+,Yb3+ Upconversion Nanocrystals. *ACS Nano* **2018**, *12* (5), 4812–4823. https://doi.org/10.1021/acsnano.8b01545.
(60) Villanueva-Delgado, P.; Biner, D.; Krämer, K. W. Judd–Ofelt Analysis of β-NaGdF4: Yb3+, Tm3+ and β-NaGdF4:Er3+ Single Crystals. *J. Lumines.* **2017**, *189*, 84–90. https://doi.org/10.1016/j.jlumin.2016.04.023.
(61) Walsh, B. M. Judd-Ofelt Theory: Principles and Practices. In *Advances in Spectroscopy for Lasers and Sensing*; Di Bartolo, B., Forte, O., Eds.; Springer Netherlands: Dordrecht, 2006; pp 403–433. https://doi.org/10.1007/1-4020-4789-4_21.
(62) Skrzypczak, U.; Pfau, C.; Seifert, G.; Schweizer, S. Comprehensive Rate Equation Analysis of Upconversion Luminescence Enhancement Due to $BaCl_2$ Nanocrystals in Neodymium-Doped Fluorozirconate-Based Glass Ceramics. *J. Phys. Chem. C* **2014**, *118* (24), 13087–13098. https://doi.org/10.1021/jp5021033.
(63) Teitelboim, A.; Tian, B.; Garfield, D. J.; Fernandez-Bravo, A.; Gotlin, A. C.; Schuck, P. J.; Cohen, B. E.; Chan, E. M. Energy Transfer Networks within Upconverting Nanoparticles Are Complex Systems with Collective, Robust, and History-Dependent Dynamics. *J. Phys. Chem. C* **2019**, *123* (4), 2678–2689. https://doi.org/10.1021/acs.jpcc.9b00161.
(64) Baride, A.; May, P. S.; Berry, M. T. Cross-Relaxation from Er3+(2H11/2,4S3/2) and Er3+(2H9/2) in β-NaYF4:Yb,Er and Implications for Modeling Upconversion Dynamics. *J. Phys. Chem. C* **2020**, *124* (3), 2193–2201. https://doi.org/10.1021/acs.jpcc.9b10163.
(65) Kraft, M.; Würth, C.; Muhr, V.; Hirsch, T.; Resch-Genger, U. Particle-Size-Dependent Upconversion Luminescence of NaYF4: Yb, Er Nanoparticles in Organic Solvents and Water at Different Excitation Power Densities. *Nano Res.* **2018**, *11* (12), 6360–6374. https://doi.org/10.1007/s12274-018-2159-9.
(66) Rabouw, F. T.; den Hartog, S. A.; Senden, T.; Meijerink, A. Photonic Effects on the Förster Resonance Energy Transfer Efficiency. *Nat. Commun.* **2014**, *5* (1), 3610. https://doi.org/10.1038/ncomms4610.

(67) Senden, T.; Rabouw, F. T.; Meijerink, A. Photonic Effects on the Radiative Decay Rate and Luminescence Quantum Yield of Doped Nanocrystals. *ACS Nano* **2015**, *9* (2), 1801–1808. https://doi.org/10.1021/nn506715t.

(68) Bhuckory, S.; Hemmer, E.; Wu, Y.-T.; Yahia-Ammar, A.; Vetrone, F.; Hildebrandt, N. Core or Shell? Er3+ FRET Donors in Upconversion Nanoparticles. *Eur. J. Inorg. Chem.* **2017**, *2017* (44), 5186–5195. https://doi.org/10.1002/ejic.201700904.

(69) Wang, Y.; Liu, K.; Liu, X.; Dohnalová, K.; Gregorkiewicz, T.; Kong, X.; Aalders, M. C. G.; Buma, W. J.; Zhang, H. Critical Shell Thickness of Core/Shell Upconversion Luminescence Nanoplatform for FRET Application. *J. Phys. Chem. Lett.* **2011**, *2* (17), 2083–2088. https://doi.org/10.1021/jz200922f.

(70) Noculak, A.; Podhorodecki, A.; Pawlik, G.; Banski, M.; Misiewicz, J. Ion–Ion Interactions in β-$NaGdF_4$:Yb^{3+},Er^{3+} Nanocrystals – the Effect of Ion Concentration and Their Clustering. *Nanoscale* **2015**, *7* (32), 13784–13792. https://doi.org/10.1039/C5NR03385C.

(71) Meijer, M. S.; Natile, M. M.; Bonnet, S. 796 Nm Activation of a Photocleavable Ruthenium(II) Complex Conjugated to an Upconverting Nanoparticle through Two Phosphonate Groups. *Inorg. Chem.* **2020**, *59* (20), 14807–14818. https://doi.org/10.1021/acs.inorgchem.0c00043.

(72) Estebanez, N.; González-Béjar, M.; Pérez-Prieto, J. Polysulfonate Cappings on Upconversion Nanoparticles Prevent Their Disintegration in Water and Provide Superior Stability in a Highly Acidic Medium. *ACS Omega* **2019**, *4* (2), 3012–3019. https://doi.org/10.1021/acsomega.8b03015.

(73) Zhao, J.; Lu, Z.; Yin, Y.; McRae, C.; Piper, J. A.; Dawes, J. M.; Jin, D.; Goldys, E. M. Upconversion Luminescence with Tunable Lifetime in NaYF4:Yb,Er Nanocrystals: Role of Nanocrystal Size. *Nanoscale* **2013**, *5* (3), 944–952. https://doi.org/10.1039/C2NR32482B.

(74) Vaitkus, A.; Merkys, A.; Gražulis, S. Validation of the Crystallography Open Database Using the Crystallographic Information Framework. *J. Appl. Cryst.* **2021**, *54* (2), 661–672. https://doi.org/10.1107/S1600576720016532.

(75) Grzechnik, A.; Bouvier, P.; Mezouar, M.; Mathews, M. D.; Tyagi, A. K.; Köhler, J. Hexagonal Na1.5Y1.5F6 at High Pressures. *J. Solid State Chem.* **2002**, *165* (1), 159–164. https://doi.org/10.1006/jssc.2001.9525.

(76) Roy, D. M.; Roy, R. Controlled Massively Defective Crystalline Solutions with the Fluorite Structure. *J. Electrochem. Soc.* **1964**, *111* (4), 421. https://doi.org/10.1149/1.2426145.

TOC image